scientific reports

OPEN

Inverse-cavity structure for low-threshold miniature lasers

Gunpyo Kim, Seok Ho Song & Jae Woong Yoon✉

Creating micro and nano lasers, high threshold gain is an inherent problem that have critically restricted their great technological potentials. Here, we propose an inverse-cavity laser structure where its threshold gain in the shortest-cavity regime is order-of-magnitude lower than the conventional cavity configurations. In the proposed structure, a resonant feedback mechanism efficiently transfers external optical gain to the cavity mode at a higher rate for a shorter cavity, hence resulting in the threshold gain reducing with decreasing cavity length in stark contrast to the conventional cavity structures. We provide a fundamental theory and rigorous numerical analyses confirming the feasibility of the proposed structure. Remarkably, the threshold gain reduces down by a factor ~ 10^{-3} for a vertical-cavity surface-emitting laser structure and ~ 0.17 for a lattice-plasmonic nanocavity structure. Therefore, the proposed approach may produce extremely efficient miniature lasers desirable for variety of applications potentially beyond the present limitations.

Miniature lasers have led to far-reaching technological advances for variety of application areas including telecommunications, data processing, medical detection, and display to mention a few[1–4]. Since the invention of vertical-cavity surface-emitting laser (VCSEL)[5], extensive study on miniature lasers has been conducted to create various promising structure classes such as whispering-gallery microcavities[6], photonic crystal defect-mode cavities[7], and synthetic nanowire resonators[8]. Further miniaturization has been proposed in terms of surface-plasmonic resonance structures to take advantages of sub-diffraction-limited optical confinement and ultrafast dynamics in femtosecond time scales[9–11].

Along this line, miniaturization of lasers has continuously raised formidable challenges including high threshold gain. Compared with macroscopic lasers, micro and nano lasers require very high material gain in order to compensate remarkably increased radiative losses over a much shorter optical path length. Consequently, desired laser operation often involves extreme conditions[12–14] in material processing, temperature management, and pump controls even with the most-efficient gain media such as organic dyes[15] and semiconductors[16].

In this paper, we propose an inverse-cavity structure for micro or nano laser operation in remarkably low threshold-gain conditions. The proposed inverse-cavity structure consists of a passive cavity enclosed by amplified-feedback mechanisms, which is in an exactly opposite configuration to conventional laser structures with an amplifying cavity and dissipative feedback mechanisms. In this inverse-cavity configuration, modal amplification rate increases with decreasing cavity length as the amplified feedback events occur more frequently in a shorter cavity. Therefore, the proposed cavity structure yields lower threshold gain for a shorter cavity in stark contrast to the conventional cavity configurations. We provide a fundamental theory, efficient method to produce an amplified-feedback effect by means of nanophotonic resonances, and rigorous numerical calculations for experimentally conceivable vertical-cavity surface-emitting laser (VCSEL) and lattice-plasmonic nanocavity structures. Intriguingly, we theoretically obtain threshold-gain reduction from the conventional cavity configuration by a factor 10^{-3} for an AlGaAs VCSEL structure and 0.17 for an Au-InGaAs lattice-plasmonic laser structure in their shortest-cavity conditions. Therefore, our result suggests a promising approach for creating extremely low-threshold miniature laser elements.

Results

Fundamental theory.

A common basic structure of conventional lasers consists of a leaky resonant cavity containing a gain medium. Such a cavity structure implies minimally conceivable cavity length

$$L_c = \frac{\ln \eta_f^{-1}}{2(G_{\max} - \alpha)}, \quad (1)$$

where $G_{\max}$ is the maximum modal-gain constant obtainable from the gain medium, α is modal dissipation rate, and η_f is power efficiency of the feedback mechanism for one optical roundtrip inside the cavity. The inverse

Department of Physics, Hanyang University, Seoul 04763, Korea. ✉email: yoonjw@hanyang.ac.kr

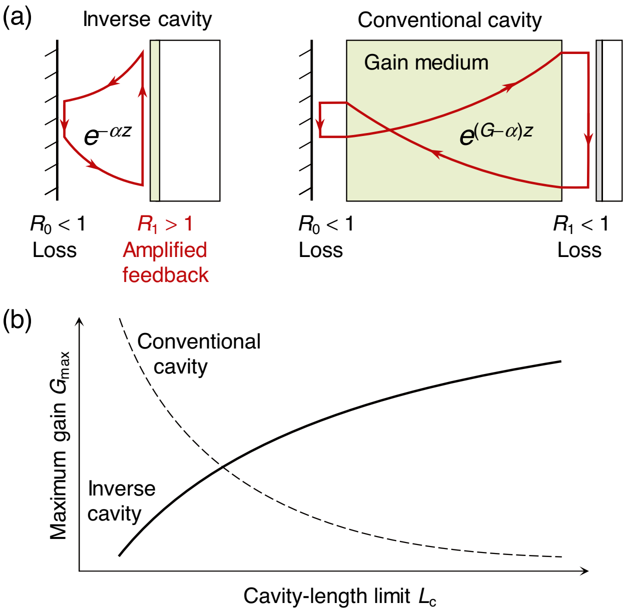

Figure 1. Inverse-cavity concept in comparison with the conventional cavity configuration. (**a**) Structure configuration of an inverse cavity versus a conventional cavity. Arrowed loops indicate instantaneous optical intensity during one roundtrip at lasing threshold. (**b**) Relation between minimal cavity length limit L_c and maximum gain constant $G_{\max}$ for an inverse-cavity structure in comparison with a conventional cavity structure.

proportionality between L_c and $G_{\max}$ is an essential consequence because the number of dissipative feedback events per unit time and subsequent radiative losses increase as the cavity becomes shorter. Consequently, reducing L_c to a certain required level for micro and nano lasers in the wavelength or subwavelength scales involves very high $G_{\max}$ or η_f at the cost of extreme controls in temperature, pumping density, and precise formation of feedback mechanisms[12–14].

In search of possible solutions to this inherent problem, we consider an inverse-cavity structure where optical gain is provided by a coherently amplified feedback mechanism instead of an intracavity gain medium, as shown in Fig. 1a in comparison with a conventional cavity configuration. In this inverse-cavity structure, we assume the amplified feedback mechanism provides feedback efficiency $\eta_f = R_0 R_1 > 1$ so that it compensates attenuation $\exp(-2\alpha L_c)$ during passive intracavity propagation. In stark contrast to the conventional cavity configuration, this inverse-cavity structure implies lower required optical gain for a shorter cavity because the cavity mode acquires higher gain for a shorter cavity by providing more frequent amplified feedback events.

Considering the gain–loss balance for stationary optical oscillation in an inverse-cavity structure, the threshold condition for amplified reflectance R_1 is

$$R_1 = \frac{1}{R_0} \exp(2\alpha L_c). \tag{2}$$

Since the threshold R_1 exponentially decreases with reducing L_c, the required optical gain $G_{\max}$ implicitly related to R_1 should also decrease for smaller L_c, as schematically illustrated in Fig. 1b. Therefore, the proposed inverse-cavity structure can be remarkably efficient especially for short-cavity lasers.

The amplified-feedback mechanism is a key component in this inverse-cavity laser concept. It is conveniently obtainable by using resonant optical scattering in various nanophotonic structures. Resonant nanophotonic scattering in many cases can be treated as a two-channel Fano-resonance problem that describes reflection coefficient r_1 as a superposition of non-resonant reflectivity r_D and resonant reflectivity r_R, as schematically illustrated in Fig. 2a. A generic temporal coupled-mode theory for this two-channel resonance problem[17] predicts the reflectance ($R_1 = |r_1|^2$) spectrum depending on net modal-gain constant, as shown in Fig. 2b. We indicate net modal gain constant $G_B - \alpha_B$ relative to radiative attenuation constant α_{rad}, where G_B and α_B are modal gain and absorption constant for the leaky bound state. Maximum reflectance $R_{\max}$ exceeds 1 for $G_B - \alpha_B > 0$, indicating the amplified reflection required for the inverse-cavity laser operation.

In particular, $R_{\max}$ in the small-signal approximation is determined by

$$R_{\max} \approx 1 + C_1 \frac{G_B - \alpha_B}{\alpha_{rad} - (G_B - \alpha_B)} + C_2 \left[\frac{G_B - \alpha_B}{\alpha_{rad} - (G_B - \alpha_B)} \right]^2, \tag{3}$$

where dimensionless coefficients C_1 and C_2 are functions of resonance coupling rates, $|r_D|$, and the phase difference between r_R and r_D. See Supplementary Note I for details of the derivation based on a geometric representation of Fano-resonance scattering amplitudes. Obviously, the amplified reflection ($R_{\max} > 1$) is obtainable in

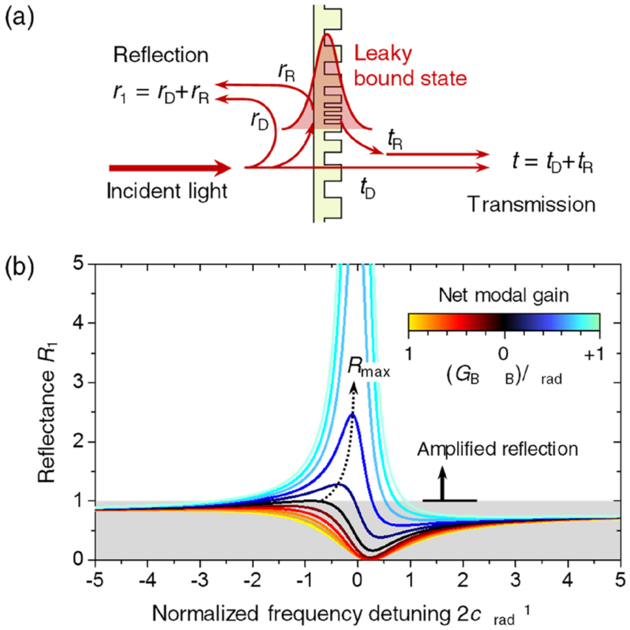

Figure 2. Amplified reflection from a nanophotonic resonance element. (**a**) Schematic illustration of two-channel resonant scattering due to a leaky bound state in a nanophotonic structure. r_R and t_R represent coefficients of the resonant reflection and transmission through a leaky bound state while the non-resonant scattering is described by r_D and t_D. The reflectivity r_1 and transmissivity t are coherent superpositions of these resonant and non-resonant pathways. (**b**) Amplified reflection $R_1 = |r_1|^2 = |r_D + r_R|^2$ spectra for increasing net modal gain $G_B - \alpha_B$ from $-\alpha_{rad}$ to $+\alpha_{rad}$, where G_B, α_B, and α_{rad} represent modal gain, absorption, and radiative decay constants, respectively. In this calculation, we assume non-resonant reflectance $|r_D|^2 = 0.8$, non-resonant transmittance $|t_D|^2 = 1 - |r_D|^2 = 0.2$, and radiative-decay probability toward the reflection channel $\eta_1 = 0.7$ for a certain presumable example.

the leaky-bound-state amplification regime for $G_B - \alpha_B > 0$. Considering an inverse-cavity laser that employs the amplified reflection from a leaky bound-state resonance in the short cavity ($\alpha L_c < < 1$) and high back-reflection ($R_0 \approx 1$) limits, the threshold condition in Eq. (2) combined with Eq. (3) predicts L_c such that

$$L_c \approx \alpha^{-1}\left[C_1\frac{(G_B - \alpha_B)}{\alpha_{rad}} + (C_1 + C_2)\frac{(G_B - \alpha_B)^2}{\alpha_{rad}^2}\right]. \tag{4}$$

Therefore, threshold modal-gain constant $G_B - \alpha_B$ required for an inverse-cavity laser operation decreases as the cavity gets shorter.

Use of a resonant reflector as the amplified feedback mechanism suggests another advantage in the optical coherence of output light because of a doubly resonant arrangement of the structure. The lasing mode in the proposed inverse-cavity structure oscillates in both the mode-selecting cavity and resonant reflector simultaneously. Every feedback event inside the mode-selecting cavity involves resonant excitation of a leaky bound state in the amplifying reflector. Therefore, photon density N_R in the resonant reflector containing the gain medium is substantially enhanced from photon density N_C in the mode-selecting cavity such that $N_R \approx (2\pi D/\lambda)^{-1} Q_R \cdot N_C$, where D is thickness of the resonant reflector, λ is wavelength of light, and Q_R is resonance quality factor of the resonant reflector. This implies that the stimulated emission rate in the gain medium is enhanced by a factor ~ $(2\pi D/\lambda)^{-1} Q_R$ from that expected if the gain medium was contained in the mode-selecting cavity. Therefore, an inverse-cavity laser can produce output light with substantially higher coherence than conventional cavity structures with the mode-selecting cavity being in a similar length scale.

Numerical analysis. In order to see if the proposed inverse-cavity structure produces remarkably low-threshold laser oscillation in practical systems, we perform rigorous numerical analyses on two distinct nanophotonic cavity structures. They are VCSEL and lattice-plasmonic cavity structures.

In the VCSEL structure study, we compare a conventional VCSEL and inverse-cavity structures based on AlGaAs-compound multilayer system as shown in Fig. 3a. In the inverse-cavity structure, the top distributed-Bragg-reflection (DBR) multilayer in the conventional VCSEL structure is replaced by a GaAs guided-mode-resonance (GMR) reflector that provides desired amplified feedback towards the AlAs passive cavity. Considering emission wavelength around 800 nm from GaAs as a gain medium, we assume a trial case with parameters indicated in the figure caption. We include complex refractive index $2.95 + i1.6 \times 10^{-4}$ for the AlAs passive cavity and $3.6 + i\kappa$ for the GaAs GMR reflector layer, where extinction coefficient κ yields net material gain constant

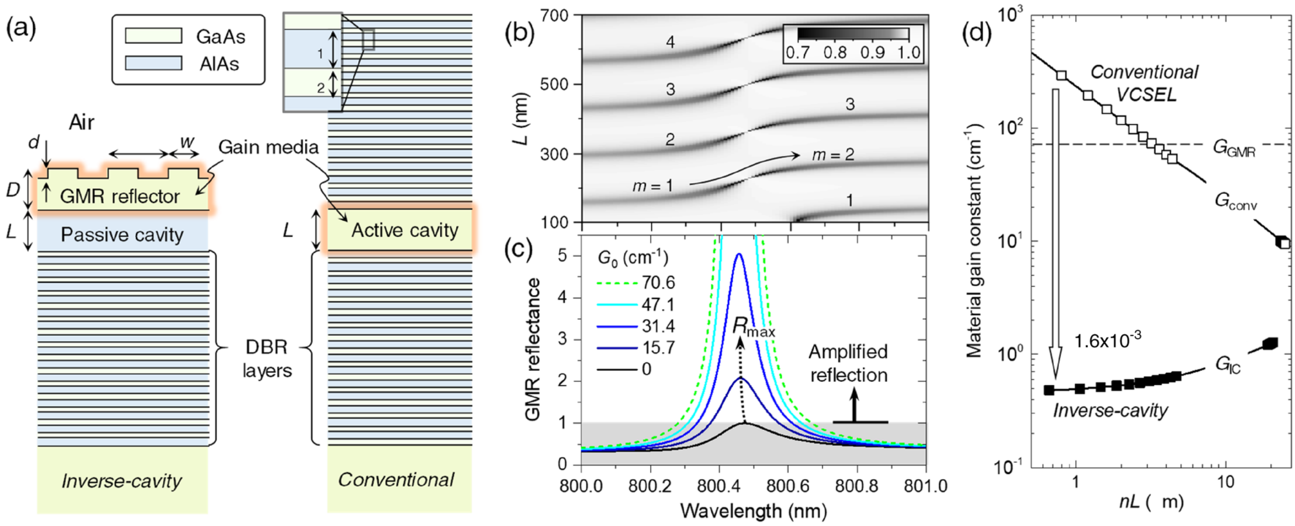

Figure 3. VCSEL employing an inverse-cavity structure. (**a**) Geometry of a GaAs-AlAs-based inverse-cavity structure in comparison with a conventional VCSEL structure. Optical gain is applied to the GaAs guided-mode-resonance (GMR) reflector for the inverse-cavity structure and GaAs Fabry-Pérot cavity for the conventional VCSEL structure. (**b**) Reflectance spectrum on L-λ plane for an inverse-cavity structure under normal incidence from the air cover. Geometrical parameters and optical constants are $d = 25$ nm, $D = 475$ nm, $\Lambda = 226.5$ nm, $w = \Lambda/2$, $\delta_1 = 67.8$ nm, $\delta_2 = 55.6$ nm, and refractive indices 2.95 for AlAs and 3.6 for GaAs. Material gain constant $G_0 = 0$ in the GaAs GMR reflector for this spectrum and m denotes a Fabry-Pérot (FP) order. (**c**) Amplified internal reflectance spectra due to a gain-assisted GMR for increasing G_0. (**d**) Calculated threshold gain constants G_{IC} for the inverse-cavity structure and G_{conv} for the conventional VCSEL structure as functions of cavity optical path length nL. G_{GMR} is threshold gain constant for the GMR in the absence of the bottom DBR layers ($L = \infty$).

$G_0 = -(4\pi/\lambda)\kappa$ with λ being wavelength of light in vacuum. We use the rigorous coupled-wave analysis (RCWA)[18] for numerical calculation.

In Fig. 3b, we show normal-incidence reflectance spectrum of the inverse-cavity structure on wavelength (λ) and cavity length (L) domain that reveals cavity-resonance condition under the influence of the resonant reflection from the GMR reflector layer for $G_0 = 0$. The cavity resonances create periodic dark minima labeled by order m indicating the number of field oscillation during one intracavity roundtrip as in the canonical Fabry-Pérot (FP) resonators. The resonant internal reflection from the GMR layer leads to two characteristic features in these cavity resonance minima. One is the FP order shift from m to $m + 1$. This is caused by resonant 2π-phase change in the internal reflection over a narrow GMR band from 800.2 to 800.8 nm. The second characteristic feature is vanishingly narrow resonance linewidth in the middle of the order shift region, *i.e.*, cavity resonances at $\lambda = 800.476$ nm. This is a bound state in the continuum (BIC) appearing as radiative decay towards the air cover vanishes at the internal reflectance maximum ($R_{max} = 1$) condition.

As G_0 in the GMR layer increases from zero, the internal reflection is amplified ($R_{max} > 1$) as shown in Fig. 3c and the BIC features for different FP orders at $\lambda = 800.476$ nm can oscillate as lasing modes presumably with a minimal threshold gain constant. Considering attenuation $\alpha = 25.12$ cm^{-1} inside the AlAs cavity and DBR reflectance $R_0 = 0.9899$, radiative decay rate $\alpha_{rad} = 70.6$ cm^{-1} of the GMR, and GMR's radiative decay probability $\eta_1 \approx 0.6$ toward the AlAs cavity in our specific case here, we estimate an inverse-cavity threshold gain constant $G_0 = G_{IC} \approx 0.46$ cm^{-1} for the lowest-order BIC mode at $\lambda = 800.476$ nm and $L = 224$ nm from Eqs. (2) and (3) in an ideal case for $G_0 = G_B - \alpha_B$. Remarkably, Eq. (1) for the conventional VCSEL structure with the same cavity length yields a threshold gain constant $G_0 = G_{conv} \approx 474$ cm^{-1}, which is remarkably higher from G_{IC} by a factor around 10^3.

In order to better substantiate this intriguing property, we numerically calculate threshold gain constants G_{IC} and G_{conv} by using a G_0-dependent resonance-excitation spectrum analysis, as provided in Supplementary Note II. Therein, we determine the threshold gain constant to be a G_0 value for a scattering-matrix pole at which bandwidth of the resonance-excitation spectrum vanishes and its peak value diverges to the infinity. This frequency-domain analysis has been used to estimate ideal threshold gain constant that compensates necessary cavity losses[19,20]. However, it does not account for material dispersion and gain saturation nonlinearity and thereby cannot predict linewidth and intensity beyond the threshold condition. In spite of such limitations, the frequency-domain analysis provides a reasonable comparison for the fundamentally required threshold gain constant which is our major interest here.

In Fig. 3d, we show the result obtained as a function of cavity optical path length nL, where n is real-part refractive index of the cavity medium. In this result, G_{IC} for the inverse-cavity structure decreases for smaller L in contrast to increasing G_{conv} for the conventional VCSEL structure, as predicted in the previous section. For the lowest-order inverse-cavity mode at $L = 224$ nm as the shortest laser cavity, $G_{IC} = 0.48$ cm^{-1} $\approx 1.6 \times 10^{-3} \cdot G_{conv}$. Notably, G_{IC} is also considerably lower than $G_{GMR} = \alpha_{rad} = 70.6$ cm^{-1} $\approx 1.5 \times 10^2 \cdot G_{IC}$, which is threshold gain constant for the GMR reflector itself as a second-order distributed-feedback (DFB) laser in the absence of the bottom DBR.

In further consideration on the property $G_{\mathrm{IC}} < < G_{\mathrm{GMR}}$, G_{IC} is essentially lower than G_{GMR} because G_{IC} is reached at a condition for an amplified reflectance at a certain finite level while G_{GMR} is obtained when the amplified reflectance tends to the infinity as a pole in the scattering matrix of the GMR reflector itself. Looking into this aspect in connection with Eqs. (2) and (3), we derive an expression for threshold gain-constant ratio

$$M \equiv \frac{G_{\mathrm{IC}}}{G_{\mathrm{GMR}}} = \frac{G_{\mathrm{B}}^{(\mathrm{IC})} - \alpha_{\mathrm{B}}}{G_{\mathrm{B}}^{(\mathrm{GMR})} - \alpha_{\mathrm{B}}} = \frac{1}{1+\xi}. \tag{5}$$

Here, $\xi = 2C_2[\{C_1{}^2 + (4\alpha L_c)C_2\}^{1/2} - C_1]^{-1}$. See Eq. (S3) in Supplementary Note I for expressions of coefficients C_1 and C_2. Importantly, ξ is always a positive number and $M < 1$. This implies that if G_{GMR} is substantially reduced down by additional optimization for a better DFB laser property, inclusion of it as an amplified reflector for an inverse-cavity laser necessarily results in a lower threshold gain G_{IC} than G_{GMR}. Therefore, our trial case analysis clearly demonstrates the desired advantage of the inverse-cavity laser concept over the conventional systems such as VCSEL and second-order DFB laser structures.

Although the low threshold gain-constant property takes many advantages in laser operation, it is important to estimate lateral footprint size of the cavity and consequent net pumping power requirement. Comparing the proposed inverse-cavity and conventional VCSEL designs in Fig. 3, we calculate angular full-width at half maximum of the cavity modes for both structures and estimate their corresponding diffraction-limited beam sizes as the minimally possible footprint size W_{min} of the cavity. We obtain $W_{\mathrm{IC}} = 2.5$ mm for W_{min} in the inverse-cavity design and $W_{\mathrm{conv}} = 13.5$ μm for W_{min} in the conventional VCSEL design. Threshold pumping power ratio is then roughly estimated as $(W_{\mathrm{IC}}/W_{\mathrm{conv}})^2 \cdot (G_{\mathrm{IC}}/G_{\mathrm{conv}}) \approx 55$, implying that the proposed inverse cavity strucrture requires significantly higher pumping power as a result of the inevitably large footprint size. Therefore, additional footprint-size reduction scheme should be introduced in order to take full advantages of the low threshold gain constant property.

There are several available methods for reducing lateral size of GMR reflector structures without substantial loss in the feedback efficiency[21]. They are mainly based on additional first-order distributed feedback gratings[22] on the side edges and doubly-periodic GMR designs[23]. For example, we conduct a trial numerical analysis for an inverse-cavity configuration based on a doubly-periodic GMR design, as explained in Supplementary Note III. Therein, we obtain $G_{\mathrm{IC}} = 1.33\ \mathrm{cm}^{-1} \approx 2.9 \times 10^{-3} \cdot G_{\mathrm{conv}}$ and $W_{\mathrm{IC}} = 172.7$ μm $\approx 12.8 \cdot W_{\mathrm{conv}}$. Threshold pumping power ratio is then roughly estimated as $(W_{\mathrm{IC}}/W_{\mathrm{conv}})^2 \cdot (G_{\mathrm{IC}}/G_{\mathrm{conv}}) \approx 0.47$, implying that the threshold pumping power is a half of that for the conventional VCSEL structure. According to Ref. 21, the minimum footprint size of doubly periodic GMR reflectors is in the order of $10 \times 10\ \mu\mathrm{m}^2$ and this corresponds to a typical footprint size of conventional VCSEL structures. Therefore, the low threshold property of an inverse-cavity structure should be sustainable without significant increase in the footprint size or threshold pumping power if a certain optimized size-reduction scheme is introduced in the resonant reflector design.

We further investigate feasibility of the inverse-cavity structure for plasmonic lasers which potentially enable extremely small lasers taking advantages of deep subwavelength confinement and ultrafast dynamic properties[24]. We consider a periodic array of metal–insulator-metal (MIM) nanocavities in an Au-InGaAs-InP system as shown in Fig. 4a. In this specific geometry, the nano-slit cavities support FP-like resonances of metal–insulator-metal plasmonic guided modes, *i.e.*, cavity modes, and the Au-InGaAs interface accommodates surface-plasmon polaritons (SPP) which can be amplified by the stimulated SPP emission from coherent carrier recombination in the InGaAs layer. Hence, the internal reflection of the cavity plasmonic modes can be amplified by mediation of amplified SPPs under certain appropriate resonant-coupling conditions similar to the inverse-cavity VCSEL structure in Fig. 3.

Considering optical emission around $\lambda = 1550$ nm from the InGaAs layer, we take geometrical parameters as indicated in the caption of Fig. 4. We assume material gain constant $G_0 = -(4\pi/\lambda)\kappa$ only in the InGaAs layer between Au-InGaAs and InGaAs-InP interfaces in order to exclude direct amplification of the cavity-plasmonic modes in this proof-of-concept numerical analysis. In Fig. 4b, we reveal cavity-plasmonic resonance conditions from reflectance spectrum of the structure for $G_0 = 0$ under normal light incidence from the InP cover. The periodic resonance dips are due to FP-like resonances of the cavity-plasmonic modes. In the similar manner to the previous VCSEL case, these cavity-plasmonic resonances also include the FP-order shift and BIC states around 1550 nm in response to the resonant internal reflection with SPP excitation in the second-order Bragg reflection regime.

Amplified internal-reflection spectrum from the gain-assisted SPP resonance is provided in Fig. 4c as a function of G_0. For $G_0 = 0$, the characteristically asymmetric Fano-resonance profile has a minimum at $\lambda = 1440$ nm and maximum $R_{\mathrm{max}} \approx 1$ at $\lambda = 1550$ nm where the BIC features in Fig. 4b appear at. As G_0 increases, R_{max} is amplified from 1 and its spectral location shifts towards the SPP-resonance excitation center at $\lambda = 1480$ nm. For $G_0 = 2 \times 10^4\ \mathrm{cm}^{-1}$, R_{max} diverges to the infinity and we take this value as threshold gain constant G_{SPP} for the SPP as a second-order DFB lasing mode in our specific case here.

The blue shift of the R_{max} wavelength with increasing G_0 pushes the lowest-gain inverse-cavity lasing wavelength for the cavity-plasmonic modes towards slightly shorter wavelength from the BIC point at $\lambda = 1550$ nm. Hence, we select $\lambda = 1510$ nm (dashed line in Fig. 4b) as an approximate optimal point and numerically determine threshold gain constant G_{CP} for each cavity-plasmonic FP-like resonance feature by using the G_0-dependent resonance-excitation spectrum analysis as used in the previous VCSEL case. The result is provided in Fig. 4d. Calculated G_{CP} shows a desired linear dependence on cavity length L as expected for inverse-cavity laser structures in general. For the lowest FP order at $L = 130$ nm, $G_{\mathrm{CP}} = 3.52 \times 10^3\ \mathrm{cm}^{-1}$, which is only about 1/6 of G_{SPP} in spite of stronger absorption losses in the plasmonic cavity mode. Moreover, G_{CP} is only 1/5.5 of a threshold gain constant $1.93 \times 10^4\ \mathrm{cm}^{-1}$ for direct amplification of a plasmonic cavity mode at the lowest FP order in the

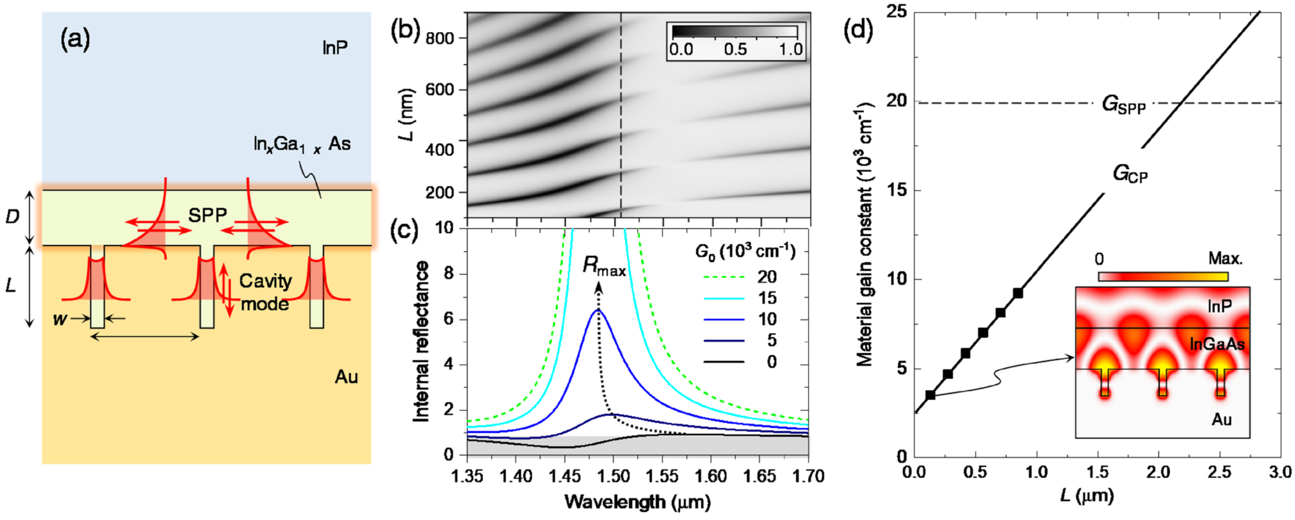

Figure 4. Plasmonic inverse-cavity laser property. (**a**) Structure geometry of an Au-InGaAs-based plasmonic inverse-cavity structure where periodic nanoslits function as plasmonic nanocavities and resonant grating for SPPs on the Au-InGaAs interface. (**b**) Reflectance spectrum on L-λ plane for a plasmonic inverse-cavity structure under normal incidence from the InP cover. Geometrical parameters $\Lambda = 410$ nm, $w = 50$ nm, $D = 200$ nm. We take frequency-dispersive optical constants of InP[25], InGaAs[26], and Au[27] from the literature in consideration of relatively wide spectral range of the plasmonic resonance effects in our present case. (**c**) Amplified internal reflectance spectra due to a gain-assisted SPP resonance for increasing G_0. (**d**) Calculated threshold gain constants G_{CP} for the plasmonic inverse-cavity structure as functions of cavity length L. G_{SPP} is threshold gain constant for the SPP resonance on the Au-InGaAs interface for open cavities with $L = \infty$.

absence of the gain-assisted SPP resonance. Therefore, the inverse-cavity approach can create remarkably efficient plasmonic lasers under appropriate design schemes.

We note that lasing modes in an inverse-cavity structure are in a hybrid nature because cavity modes essentially excites a resonant mode associated with the amplified reflection. For example, the inset of Fig. 4d shows magnetic field intensity distribution for the lowest FP-order cavity-plasmonic resonance at $L = 130$ nm. We see that a standing SPP mode at the Au-InGaAs interface placing its anti-node at the cavity mouth is strongly excited along with the FP-like cavity-plasmonic mode resonance. Accordingly, this type of laser may not fully exploit strong cavity-QED effects for deep-subwavelength plasmonic modes. Nevertheless, careful trade-off of this restriction with the advantage of low threshold lasing may yield optimal designs required for specific applications.

Discussion

In conclusion, we have numerically demonstrated the inverse-cavity laser structures for their unusually low threshold-gain property in the shortest cavity regime. The proposed inverse-cavity amplification mechanism yields thousand times lower threshold gain in a conceivable VCSEL structure than the conventional approach and reduces threshold gain of a lattice plasmonic nanocavity laser by almost one order of magnitude.

In our proposed inverse-cavity structure, a key essential component is the amplified-feedback mechanism and it is obtainable with a gain medium involving nanophotonic resonance structures. Although we have treated strictly periodic structures in this proof-of-concept analysis, the proposed approach is in principle applicable for non-periodic cases where various beam control schemes can be included on demand. For example, in VCSEL structures, cross-sectional beam intensity, phase, and polarization profiles can be engineered by appropriately tapering geometrical parameters of a GMR reflector design to produce desired distributions such as super-Gaussian flat-top beams[28], long depth-of-focus Bessel beams[29], polarization vector beams[30], orbital angular-momentum modes[31], and many others. Therefore, it is of our great interest to derive and realize various periodic and non-periotic inverse-cavity laser designs taking advantages of low threshold gain and beam control capabilities.

Data availability

All data generated or analyzed during this study are included in this published article (and its supplementary information files SI).

Received: 3 February 2022; Accepted: 22 June 2022
Published online: 05 July 2022

References

1. Smit, M., Van der Tol, J. & Hill, M. Moore's law in photonics. *Laser Photonics Rev.* **6**, 1–13 (2012).
2. Gather, M. C. & Yun, S. H. Single-cell biological lasers. *Nat. Photonics* **5**, 406–410 (2011).
3. Kim, T.-I. *et al.* Injectable, cellular-scale optoelectronics with applications for wireless optogenetics. *Science* **340**, 211–216 (2013).
4. Blanche, P.-A. *et al.* Holographic three-dimensional telepresence using largearea photorefractive polymer. *Nature* **468**, 80–83 (2010).

5. Lee, Y. H. *et al.* Room-temperature continuous-wave vertical-cavity single-quantum-well microlaser diodes. *Electron. Lett.* **25**, 1377–1378 (1989).
6. Levi, A. F. J. *et al.* Room temperature operation of microdisc lasers with submilliamp threshold current. *Electron. Lett.* **28**, 1010–1012 (1992).
7. Painter, O. *et al.* Two-dimensional photonic band-gap defect mode laser. *Science* **284**, 1819–1821 (1999).
8. Huang, M. H. *et al.* Room-temperature ultraviolet nanowire nanolasers. *Science* **292**, 1897–1899 (2001).
9. Hill, M. T. *et al.* Lasing in metal-insulator-metal sub-wavelength plasmonic waveguides. *Opt. Express* **17**, 11107–11112 (2009).
10. Oulton, R. F. *et al.* Plasmon lasers at deep subwavelength scale. *Nature* **461**, 629–632 (2009).
11. Noginov, M. A. *et al.* Demonstration of a spaser-based nanolaser. *Nature* **460**, 1110–1112 (2009).
12. Shen, K. C. *et al.* Deep-ultraviolet hyperbolic metacavity laser. *Adv. Mater.* **30**, 1706918 (2018).
13. Van Beijnum, F. *et al.* Surface plasmon lasing observed in metal hole arrays. *Phys. Rev. Lett.* **110**, 206802 (2013).
14. Silfvast, W. T. in *Laser fundamentals* 225–289 (Cambridge university press, 2004).
15. Song, W., Vasdekis, A. E., Li, Z. & Psaltis, D. Optofluidic evanescent dye laser based on a distributed feedback circular grating. *Appl. Phys. Lett.* **94**, 161110 (2009).
16. Chang, S. W., Lin, T. R. & Chuang, S. L. Theory of plasmonic Fabry-Perot nanolasers. *Opt. Express* **18**, 15039–15053 (2010).
17. Yoon, J. W., Jung, M. J., Song, S. H. & Magnusson, R. Analytic theory of the resonance properties of metallic nanoslit arrays. *IEEE J. Quantum Electron.* **48**, 852–861 (2012).
18. Moharam, M. G. & Gaylord, T. K. Rigorous coupled-wave analysis of planar-grating diffraction. *J. Opt. Soc. Am.* **71**, 811–818 (1981).
19. Zheludev, N. I. *et al.* Lasing spaser. *Nat. Photonics* **2**, 351–354 (2008).
20. Deng, Z. L. *et al.* Power transmission and group delay in gain-assisted plasmon-induced transparency. *AIP Adv.* **3**, 032138 (2013).
21. Gambino, F. *et al.* A review on dielectric resonant gratings: Mitigation of finite size and Gaussian beam size effects. *Res. Opt.* **6**, 100210 (2022).
22. Kintaka, K. *et al.* Cavity-resonator-integrated guided-mode resonance filter for aperture miniaturization. *Opt. Express* **20**, 1444–1449 (2012).
23. Mizutani, A., Kikuta, H. & Iwata, K. Wave localization of doubly periodic guided-mode resonant grating filters. *Opt. Rev.* **10**, 13–18 (2003).
24. Yoon, J. W., Song, S. H. & Magnusson, R. Ultrahigh-Q metallic nanocavity resonances with externally-amplified intracavity feedback. *Sci. Rep.* **4**, 1–5 (2014).
25. Pettit, G. D. & Tunner, W. J. Refractive index of InP. *J. Appl. Phys.* **36**, 2081–2081 (1965).
26. See the modified Sellmeier equation for the refractive index of $In_xGa_{1-x}As$ at https://www.batop.de/information/n_InGaAs.html. We take the refractive index for $x = 0.53$.
27. Johnson, P. B. & Christy, R. W. Optical constants of the noble metals. *Phys. Rev. B* **6**, 4370–4379 (1972).
28. Caley, A. J. *et al.* Diffractive optical elements for high gain lasers with arbitrary output beam profiles. *Opt. Express* **15**, 10699–10704 (2007).
29. Chen, W. T. *et al.* Generation of wavelength-independent subwavelength Bessel beams using metasurfaces. *Light Sci. Appl.* **6**, e16259 (2017).
30. Rosales-Guzmán, C., Ndagano, B. & Forbes, A. A review of complex vector light fields and their applications. *J. Opt.* **20**, 123001 (2018).
31. Willner, A. E. *et al.* Optical communications using orbital angular momentum beams. *Adv. Opt. Photon.* **7**, 66–106 (2015).

Acknowledgements

This work was supported by the Leader Researcher Program (NRF-2019R1A3B2068083), the research fund of Hanyang University (HY-202000000000513), and the Basic Science Research Program (NRF-2018R1A2B3002539).

Author contributions

J.W.Y. conceived the original concept. J.W.Y., G.K., and S.H.S. developed the fundamental theory. G.K. performed the numerical analyses. All authors discussed the results. J.W.Y. and G.K. wrote the manuscript.

Funding

This article was funded by National Research Foundation of Korea (NRF-2019R1A3B2068083) and Hanyang University (HY-202000000000513).

Competing interests

The authors declare no competing interests.

Additional information

Supplementary Information The online version contains supplementary material available at https://doi.org/10.1038/s41598-022-15319-y.

Correspondence and requests for materials should be addressed to J.W.Y.

Reprints and permissions information is available at www.nature.com/reprints.

Publisher's note Springer Nature remains neutral with regard to jurisdictional claims in published maps and institutional affiliations.

Open Access This article is licensed under a Creative Commons Attribution 4.0 International License, which permits use, sharing, adaptation, distribution and reproduction in any medium or format, as long as you give appropriate credit to the original author(s) and the source, provide a link to the Creative Commons licence, and indicate if changes were made. The images or other third party material in this article are included in the article's Creative Commons licence, unless indicated otherwise in a credit line to the material. If material is not included in the article's Creative Commons licence and your intended use is not permitted by statutory regulation or exceeds the permitted use, you will need to obtain permission directly from the copyright holder. To view a copy of this licence, visit http://creativecommons.org/licenses/by/4.0/.

© The Author(s) 2022